Zitierweise: *Angew. Chem. Int. Ed.* **2022,** *61,* e202206915
Internationale Ausgabe: doi.org/10.1002/anie.202206915
Deutsche Ausgabe: doi.org/10.1002/ange.202206915

H_2O_2 Synthesis

Constructing Interfacial Boron-Nitrogen Moieties in Turbostratic Carbon for Electrochemical Hydrogen Peroxide Production

Zhihong Tian[+], Qingran Zhang[+], Lars Thomsen, Nana Gao, Jian Pan, Rahman Daiyan, Jimmy Yun, Jessica Brandt, Nieves López-Salas, Feili Lai, Qiuye Li, Tianxi Liu, Rose Amal, Xunyu Lu,* and Markus Antonietti**

Abstract: The electrochemical oxygen reduction reaction (ORR) provides a green route for decentralized H_2O_2 synthesis, where a structure–selectivity relationship is pivotal for the control of a highly selective and active two-electron pathway. Here, we report the fabrication of a boron and nitrogen co-doped turbostratic carbon catalyst with tunable B–N–C configurations (CNB-ZIL) by the assistance of a zwitterionic liquid (ZIL) for electrochemical hydrogen peroxide production. Combined spectroscopic analysis reveals a fine tailored B–N moiety in CNB-ZIL, where interfacial B–N species in a homogeneous distribution tend to segregate into hexagonal boron nitride domains at higher pyrolysis temperatures. Based on the experimental observations, a correlation between the interfacial B–N moieties and HO_2^- selectivity is established. The CNB-ZIL electrocatalysts with optimal interfacial B–N moieties exhibit a high HO_2^- selectivity with small overpotentials in alkaline media, giving a HO_2^- yield of $\approx$1787 mmol $g_{catalyst}^{-1} h^{-1}$ at −1.4 V in a flow-cell reactor.

Introduction

Hydrogen peroxide (H_2O_2) as a versatile and environmentally safe oxidizing agent has garnered extensive market attention, especially in light of the COVID-19 pandemic as a disinfectant, reaching a market value of USD 1.6 billion in 2019 and is projected to increase further to around 2.1 billion by 2027.[1] Nevertheless, currently most of the H_2O_2 (>95 %) is manufactured industrially using the anthraquinone method, which requires multistep oxidation and reduction of organic precursors in an energy intensive manner, making this process neither economic nor eco-friendly.[2] Besides, the H_2O_2 is generated in a highly concentrated form through an additional distillation step after the anthraquinone approach, which inevitably poses safety concerns in the distribution and transportation of the final product.[3] Further, most end-users demand only low concentrations of peroxide agent, resulting in a mismatch between on-site applications and centralized production of H_2O_2.[4] In these regards, decentralized production of peroxide agent close to the point of consumption in a safe and energy efficient manner is highly sought after. Recently, the electrochemical oxygen reduction reaction (ORR) through a selective two-electron pathway has attracted extensive research interest as it offers great opportunities for on-site H_2O_2 generation to satisfy the above demands.[5] Moreover, if this process is powered by renewable electric-

[*] Prof. Z. Tian,[+] N. Gao, Prof. Q. Li
Engineering Research Center for Nanomaterials, Henan University
Kaifeng 475004 (P. R. China)
Dr. Q. Zhang,[+] Dr. J. Pan, Dr. R. Daiyan, Prof. J. Yun, Prof. R. Amal, Dr. X. Lu
Particles and Catalysis Research Group, School of Chemical Engineering, University of New South Wales
Sydney, New South Wales 2052 (Australia)
E-mail: qingran.zhang@unsw.edu.au
xunyu.lu@unsw.edu.au
Prof. Z. Tian,[+] J. Brandt, Dr. N. López-Salas, Prof. M. Antonietti
Department of Colloid Chemistry
Max Planck Institute of Colloids and Interfaces
14476 Potsdam (Germany)
E-mail: Office.cc@mpikg.mpg.de
Dr. L. Thomsen
Australian Synchrotron, Australian Nuclear Science and Technology Organisation
800 Blackburn Road, Clayton, VIC 3168 (Australia)
Dr. F. Lai
Department of Chemistry, KU Leuven
Celestijnenlaan 200F, 3001 Leuven (Belgium)
Prof. T. Liu
Key Laboratory of Synthetic and Biological Colloids, Ministry of Education, School of Chemical and Material Engineering, Jiangnan University
Wuxi 214122 (P. R. China)
[+] These authors contributed equally to this work.

ity, the H_2O_2 produced electrochemically can also act as a renewable oxidizing agent and contributes to decarbonization of the traditional chemical industry.[6,7] To this end, considerable efforts have been devoted to designing and developing efficient H_2O_2 synthesis systems using electrochemical methods.

The successful implementation of electrochemical H_2O_2 synthesis relies largely on developing efficient electrocatalysts that catalyze the ORR along a highly selective and active $2e^-$ pathway.[8,9] Previous reports suggest a high H_2O_2 selectivity with small overpotentials during the ORR can be achieved on some noble metals and their amalgams, such as Au, PtHg and PdHg.[10–12] However, the practical efficacy of these catalysts is severely constrained by their scarcity and possible toxicity, which far impairs them from large-scale, near consumer applications. In contrast, carbon-based materials (CMs) have recently appeared as promising candidates for H_2O_2 production due to their abundance, easily tunable catalytic properties and low cost, exhibiting low overpotentials to expedite $2e^-$ ORR while maintain a high peroxide selectivity comparable or in many cases superior to the noble-metal-based electrocatalysts.[9,13–15] In this regard, extensive research interest has been attracted into the exploration of suitable CMs that can catalyze $2e^-$ ORR efficiently and selectively, including various carbon structures with fine designed defects, oxygen functionalities, tunable porosity, active edges and heteroatom dopants.[16–22] Among them, introducing boron and nitrogen dual dopants is of particular interest to modify the CMs with desirable electrochemical properties due to the different electronegativity of B and N atoms, which conjugate into carbon skeleton that in turn changes the electronic structure of catalysts.[23] Moreover, the ternary boron carbon nitride materials formed by B/N doping are likely to possess striking performances by integrating the merits of both graphene and hexagonal boron nitride (*h*-BN).[24] In these regards, many attempts on the synthesis of B/N co-doped CMs (CNB) were reported, using fabrication strategies such as bottom-up chemical vapor deposition methods and top-down thermal annealing approaches.[25–28] However, despite significant progress, the majority of these works have only shown a $4e^-$-favored ORR process in alkaline media,[26,29–31] while that for a $2e^-$ pathway is still poorly understood. Although some theoretical simulations have indicated the possible active sites for $4e^-$ or $2e^-$ ORR in CNB materials,[32] direct experimental evidence is still missing to support those claims due to the lack of accurate control on the as-synthesized active moieties. Therefore, fine tailoring the active B–N configurations in CMs is still challenging but of paramount significance to understand the structure-selectivity relationship of CNB materials toward a two-electron ORR pathway.

Typically, in a CM containing both B and N heteroatoms, three types of atomic configurations can be formed, which are i) isolated *h*-BN domains, ii) separately located B–C and N–C bonds and iii) interfacial B–N–C moieties that are either generated on the edges of *h*-BN domains or dispersed homogeneously in a carbon skeleton.[26] Notably, due to the much higher bond energy of B–N than that of B–C and N–C, the segregation of B–N species (into *h*-BN) is thermodynamically favored during the pyrolysis, thus giving the challenges in controlling the distribution of heteroatoms.[33] For example, boric acid and NH_3 are normally employed as B and N precursors, respectively, in a post-annealing process to afford the production of CNB nanostructures on large scale.[26] Nevertheless, the dominant formation of B–N bonds is still observed during doping via this route. To achieve an increased homogeneity of B/N dopants, ion-exchange strategies were also adopted to minimize the appearance of boron nitride domains, where BO_3^- and nitrogen resins were employed as B and N sources.[34] However, metal-containing catalysts (such as $[Fe(CN)_6]^{3-}$) are required for the growth of carbon through this route, which may introduce metal impurities that would eventually affect the properties of final products.[23] To this end, achieving a controlled homogeneity of B and N dopants in carbon skeleton without metal impurities is highly desired. In recent years, ionic liquids (ILs) with charged nature have emerged as excellent precursors for doped carbon nanostructures due to their negligible volatility, molecular tunability and high thermal stability.[35–37] Besides, ILs can spontaneously form films along complex surfaces, giving opportunity to deliver a desirable homogeneity in the presence of various templates. Hence, direct pyrolysis of B/N-containing ILs shows great promise in fabricating the heteroatom-doped carbon nanostructures for various energy storage and conversion purposes. Nonetheless, despite some progress, only a few expensive cyano/nitrile-containing ILs were studied for yielding nanoporous CNB materials, leaving the exploration of such kind of catalysts with well-designed B/N active moieties behind, especially for a $2e^-$ ORR process.[37,38]

Herein, we elaborately designed an IL-assisted doping strategy to construct turbostratic two-dimensional (2D) CNB nanosheets with tunable interfacial B–N moieties for efficient electrochemical hydrogen peroxide synthesis. Using the zwitterionic liquid (ZIL), butyl-methyl-imidazol-2-ylidene borane, as a novel precursor, the B–N–C configurations on as-designed CNB materials (CNB-ZIL) could be tailored effectively by varying the pyrolysis temperatures. Notably, the charged nature of ZIL and a soft template generated by dicyandiamide precursor have led to a uniform distribution of B and N heteroatoms within the carbon skeleton, while the appearance of *h*-BN domains can be deliberately controlled. X-ray absorption spectroscopy (XAS) characterizations show the existence of homogeneously distributed B–N pairs or *h*-BN domains in CNB catalysts fabricated at different temperatures, which provides a clear chemical tool for investigating the origin of peroxide selectivity. Interestingly, experimental observations reveal a correlation between the interfacial B–N moieties and the HO_2^- selectivity. Benefited from the porous nature and the abundant interfacial B–N sites, the optimized CNB-ZIL catalyst exhibits an outstanding $2e^-$ ORR performance in alkaline media with selectivity up to 85%, delivering a HO_2^- productivity of 1787 $mmol\,g_{catalyst}^{-1}\,h^{-1}$ in a flow-cell reactor. This work provides opportunity to understand the origin of hydrogen peroxide selectivity during ORR on

heteroatom-doped carbon structures, which can be used for the design of improved catalyst materials or extended toward other reactions of interest.

Results and Discussion

As illustrated in Scheme 1, CNB-ZIL was typically synthesized through a two-step pyrolysis procedure of a mixture containing both ZIL and dicyandiamide under flowing N_2 atmosphere, where ZILs were employed as non-volatile element precursors to effectively afford a uniform B and N distribution. During the pyrolysis, it is worth noting that dicyandiamide transfers to layered graphitic carbon nitride (g-C_3N_4), which serves as a soft template for the final products.[39] Moreover, the low viscosity of ZIL promotes a uniform mixing with other ingredients throughout the high-temperature condensation, which in turn promotes the homogeneity of heteroatom dopants in the carbon framework.[40] Due to the different formation energy of B–N, B–C and N–C species, the B–N–C configurations could be fine tailored by adjusting the pyrolysis temperatures, where samples obtained at 800, 900, 1000 °C are labeled as CNB-ZIL 8, CNB-ZIL 9, and CNB-ZIL 10, respectively. It must be underlined that CNB-ZIL 8 is obtained in remarkable yield of about 44 wt %, which is above the carbonization yield of other ILs-based carbons.[41]

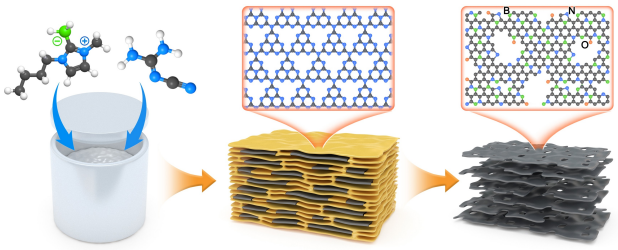

Scheme 1. Schematic illustration of synthesis procedure of CNB-ZIL catalysts.

To characterize the morphology of CNB-ZIL 8, scanning electron microscopy (SEM) was employed first. As shown in Figure S1, the CNB-ZIL exhibits an interconnected macroscopic network of nanosheets, which then forms a stacked nanoflake structure in micrometer scale. Transmission electron microscopy (TEM, Figure 1a and S2, Supporting Information) measurements confirm a scrambled nanosheet structure on CNB-ZIL 8 within numerous open pores, which might be beneficial for the effective generation of peroxide products during ORR due to a short resident time of HO_2^- in the catalysts.[42] The energy dispersive X-ray spectroscopy (EDS) elemental mapping of a selected area on the CNB-ZIL 8 exhibits uniform distributions of B, C and N elements across the nanosheet structure (Figure 1b), validating the successful incorporation of B and N atoms into the carbon matrix. To further identify the crystalline feature of B and N co-doped carbon, high-resolution TEM characterization was conducted. As shown in Figure 1c, a randomly oriented and intertwined structure could be observed, indicating a turbostratic stacking of graphitic planes with less obvious crystal-

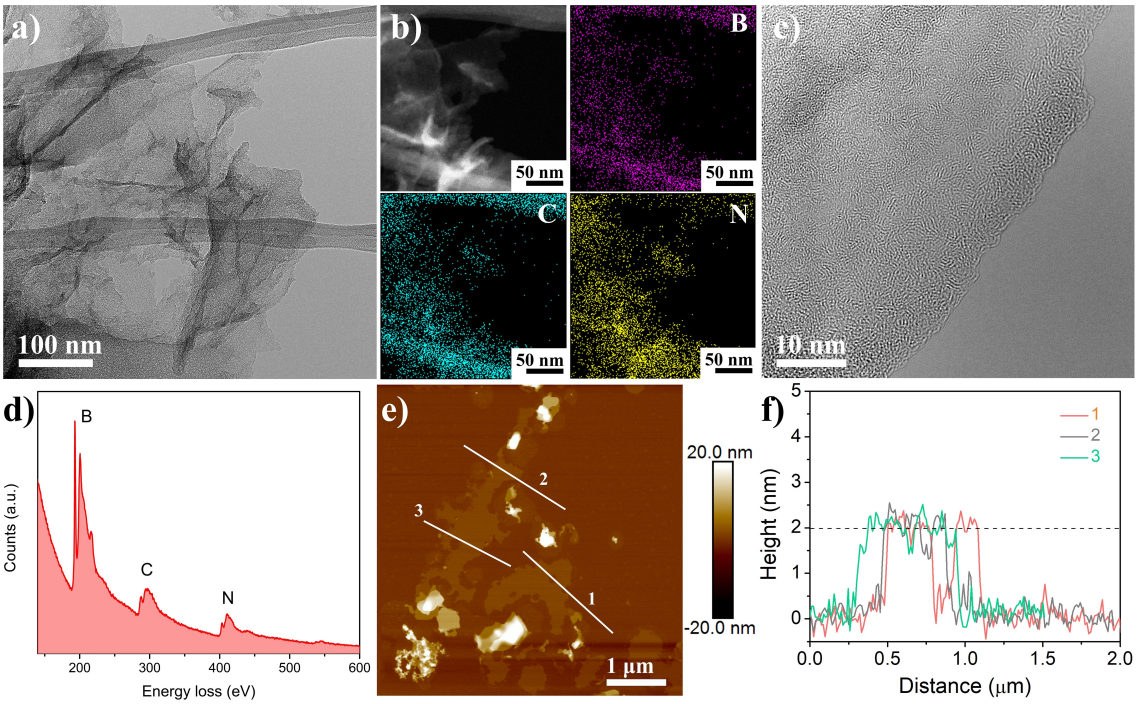

Figure 1. a) TEM image of CNB-ZIL 8. b) Scanning transmission electron microscopy (STEM) image and the corresponding EDS maps of CNB-ZIL 8 for B, C and N. c) HR-TEM image of the CNB-ZIL 8 catalysts, showing a patched turbostratic carbon structure. d) EELS point spectra of CNB-ZIL 8 catalysts. e) AFM image of CNB-ZIL 8 nanosheets and f) the height profile along the line shown in the AFM image.

line features in the CNB-ZIL 8, as supported by the selected-area reduced fast Fourier transform (FFT) pattern (Figure S3, Supporting Information). The X-ray diffraction (XRD, Figure S4, Supporting Information) further confirms the lack of obvious crystalline phases in the CNB-ZIL 8, showing no narrow Bragg reflections. Notably, the successful incorporation of B and N elements into the carbon matrix was further verified by electron energy loss spectroscopy (EELS, Figure 1d), revealing strong π* and σ* transition signals for B, N and C that indicate a highly conjugated B–N–C network.[25] The atomic force microscopy (AFM) image and corresponding height profiles of CNB-ZIL 8 (Figure 1e,f) highlight a layered 2D nanosheet structure of CNB-ZIL with a uniform thickness of ≈2 nm, corresponding to ≈4–6 structural layers of B/N co-doped graphene.[24,43,44] Thus, the above spectroscopic characterizations suggest a patched turbostratic carbon structure of CNB-ZIL 8 with a constant thickness over large areas, which is similar to the turbostratic stacking of a hybrid carbon structure as reported previously.[45] To note, the Brunauer–Emmett–Teller (BET) measurements (Figure 2a) indicate that all CNB-ZIL catalysts possess a high specific surface area, giving 525, 503 and 754 $m^2 g^{-1}$ for CNB-ZIL 8, CNB-ZIL 9 and CNB-ZIL 10, respectively. Calculated pore size distribution derived from the adsorption branch suggests surface adsorption at the layers, combined with micro- and meso slit-pores of the stacked nanosheets (Figure S5, Supporting Information). The highly organized, straight transport pores and the high specific surface area of CNB-ZIL are important to run the ORR process effectively, which not only expose more catalytically active sites but also improve the mass transfer for a rapid adsorption/desorption of reactants/products.

The chemical composition of CNB-ZIL 8 was then investigated by X-ray photoelectron spectroscopy (XPS). The corresponding XPS analyses of CNB-ZIL 9, CNB-ZIL 10 and pure boron nitride were also carried out for comparison. As shown in Figure S6 (Supporting Information), the XPS survey spectrum reveals the co-presence of B, C and N elements in the CNB-ZIL catalysts. The sum B content in CNB-ZIL 8 is calculated to be 21.2 at%, and the atomic ratio between B and N within the surface layers (less than 10 nm) is determined as ≈0.86 (Table S1, Supporting Information). Notably, the deconvolution of high-resolution XPS B 1s spectra of CNB-ZIL 8 (Figure 2b) identifies four boron components, which are 1) BC (B1, 189.0 ± 0.3 eV), 2) BNC_2 (B2, 190.3 ± 0.3 eV), 3) BN_2C (B3, 190.8 ± 0.3 eV), and 4) sp^2-BN_3 (B4, 191.6 ± 0.3 eV) species.[25,46,47] Compared with CNB-ZIL 8, the CNB-ZIL 9 and CNB-ZIL 10 materials both exhibit a substantially decreased ratio of BNC_2, while that of BN_2C and sp^2-BN_3 increases (Table S2, Supporting Information). This indicates a possible conversion of highly isolated BN pairs in the carbon substrate into more aggregated *h*-BN domains at elevated temperatures (as illustrated in Figure S7, Supporting Information). In addition, no obvious BC species can be detected in the B 1s spectra of CNB-ZIL 9 and 10, suggesting the realignment of B–C bonds under high annealing temperatures that might in turn lead to the formation of thermally more stable BN species.[32,43] This can be further confirmed by the high-resolution XPS C 1s spectra (Figure 2d), revealing the apparent disappearance of C–B bonds at 283.4 ± 0.3 eV in CNB-ZIL 9 and 10. In N1s spectra of CNB-ZIL catalysts (Figure 2c), five characteristic nitrogen peaks can be detected, assigned to i) N–B bond (N1, 397.5 ± 0.3 eV), ii) pyridinic N (N2, 398.5 ± 0.3 eV), iii) pyrrolic N (N3, 399.4 ± 0.3 eV), iv) graphitic (N4, 400.4 ± 0.3 eV) and v) inhomogeneous oxygen intercalation in the *h*-BN layers (N5, 396.7 ± 0.3 eV).[23,48] The significantly increased ratio of NC species (N2-3, Table S3, Supporting Information) in CNB-ZIL 9 and 10 clearly evidences the preferable formation of N–C bonds under high annealing temperatures, where pyridinic N becomes dominant. Collectively, from the XPS measurements, it is clear that B and N elements mainly form homogeneous B–N–C species in the CNB-ZIL 8 catalyst, which differs drastically from the dominance of highly aggregated *h*-BN and NC species in the CNB-ZIL 9 and 10. This is attributed to the larger bond energy of sp^2-hybridized BN and NC configurations, leading to segregated *h*-BN and NC domains in carbon framework under high pyrolysis temperatures.[33]

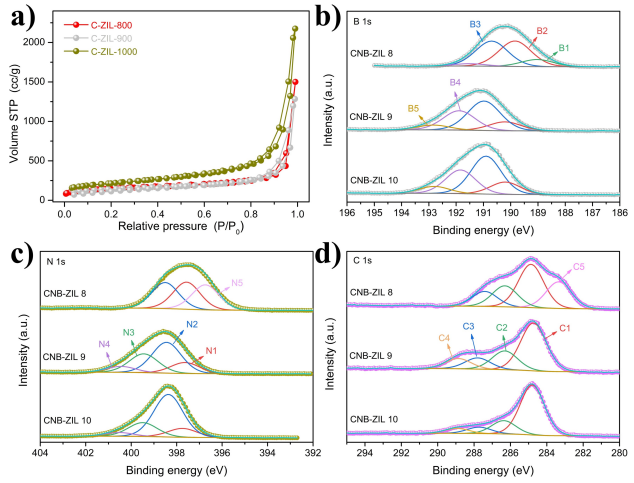

Figure 2. a) BET surface area of CNB-ZIL catalysts. High-resolution XPS b) B 1s, c) N 1s and d) C 1s spectra of CNB-ZIL 8, CNB-ZIL 9 and CNB-ZIL 10.

In order to give more in-depth understanding of the local geometric structure of B–N–C moieties in the as-prepared materials, near-edge X-ray absorption fine structure (NEXAFS) measurements were further performed. As shown in Figure 3a, the B K-edge spectrum of pure boron nitride features three characteristic peaks at 191.8, 192.5 and 193.1 eV, which can be attributed to the π* transitions of B–N bond in *h*-BN (A, e.g. BN_3), N_2BO (B) and NBO_2 (C) moieties.[48] Interestingly, the B K-edge spectra of CNB-ZIL materials all exhibit a sharp peak at 193.8 eV, corresponding to the BO_x coordination structures that mainly originate from the O_2 adsorption or intercalation.[48,49] This indicates that the oxygen molecules tend to bind to boron atoms in a BNC network due to the strong Lewis-acidity of B element, which might in turn act as the active primary adsorption sites of oxygen during the ORR catalysis. Further, the lack

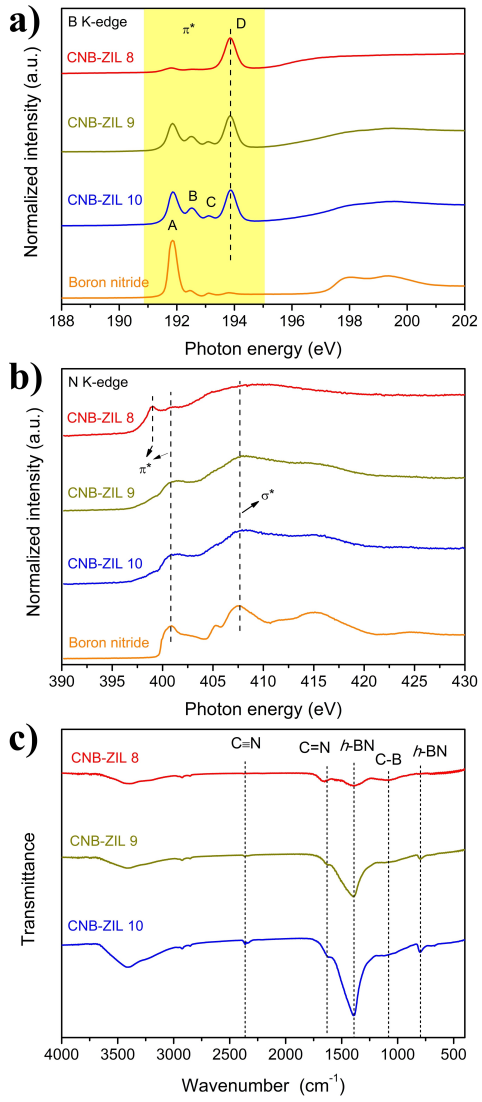

Figure 3. a) B and b) N K-edge near edge X-ray absorption fine structure (NEXAFS) spectra of the CNB-ZIL catalysts and a boron-nitride sample for comparison. c) Background-corrected FTIR spectra of CNB-ZIL catalysts.

of a sp^2-hybridized B–N feature (peak A) in the B K-edge of CNB-ZIL 8 suggests that the larger *h*-BN domains are absent in the CNB-ZIL 8 catalyst, in good agreement with the XPS measurements. In contrast, a signature *h*-BN feature similar to that of pure boron nitride was verified in the CNB-ZIL 9 and 10, giving an apparent peak A in the B K-edge spectra. Compared with CNB-ZIL 8, it is worth noting that the formation of BNO moieties (peak B and C) in CNB-ZIL 9 and 10 is ascribed to the emergence of N vacancies in a BNC substrate under high annealing temperatures. These are in the following substituted by in-plane oxygen, as also previously reported.[48,50]

Further insights were given by the N K-edge spectra of CNB-ZIL catalysts (Figure 3b), revealing a blue shift of π* transition feature at 399.0 eV for CNB-ZIL 9 and 10. Notably, the NEXFAS characterization is a sensitive probe of local bonding, thus a drastic change in the spectrum shape indicates a significant variation in the local coordination environment. Compared with the pure boron nitride, CNB-ZIL 9 and 10 show a similar π* transition peak at 400.7 eV, validating a typical *h*-BN structure with sp^2-hybridized B–N bond in these catalysts. However, such a π* transition feature downshifts to a lower photon energy side in CNB-ZIL 8, indicating the formation of a N bonding structure that is weaker than N–B in a BN_3 moiety, such as B–N–C or N–C species. Previous computational simulations suggest that a decreased BN domain size in carbon could lead to a red shift of π* peak in spectra, which is ascribed to the increased ratio of interfacial B–N–C species compared to that of N in *h*-BN centers, echoing with our observations.[51] Further performing the Fourier transform infrared spectroscopy (FTIR, Figure 3c) verifies a weak *h*-BN feature in CNB-ZIL 8, showing a small and broad peak at 1390.6 cm^{-1}, assigned to B–N stretching bands ($\nu_{B\text{-}N}$).[24] Therefore, based on the above spectroscopy measurements, it is evident that a dominant B–N–C coordination structure (e.g. BN_2C, BNC_2) has been obtained in CNB-ZIL 8, where huge *h*-BN domains are absent, resulting in a weak sp^2-BN_3 feature.

The electrocatalytic ORR performances of CNB-ZIL catalysts were firstly evaluated using a typical three-electrode rotating ring-disk electrode (RRDE) system in O_2-saturated 0.1 M KOH at room temperature. The Pt ring electrode was held at 1.2 V to quantify the amount of HO_2^- produced on the disk electrode, and a thin, uniform catalyst layer was deposited onto the glassy carbon disk electrode with a mass loading of 0.125 mg cm^{-2}. Figure 4a shows the polarization curves obtained on CNB-ZIL catalysts, with the oxygen reduction current measured on the disk electrode (solid line) and the HO_2^- oxidation current measured on the Pt ring electrode (dash line). Among all the three CNB-ZIL catalysts, CNB-ZIL 8 exhibits the highest ORR activity in terms of both current density (*j*) and onset potential (E_{onset}, defined as potential at a *j* of 0.1 mA cm^{-2}), demonstrating an advocating role of interfacial B–N–C moieties in catalyzing ORR. To be specific, with an E_{onset} of 0.8 V, obvious ORR and HO_2^- oxidation currents were detected on the disk (j_{disk}) and ring (j_{ring}) electrodes, respectively, indicating a genuine peroxide generation behavior. Moreover, along with an increased overpotential (η), the j_{disk} increases accordingly, reaching 3 mA cm^{-2} at 0 V, which is close to the theoretical mass transport limit for the $2e^-$ ORR process under 1600 rpm. Notably, the samples with obvious *h*-BN features (CNB-ZIL 9 and 10) exhibit similar E_{onset} values ($\approx$0.76 V), suggesting the presence of similar active sites within these materials. Compared with CNB-ZIL 9 ad 10, CNB-ZIL 8 shows a much lower Tafel slope (Figure S8, Supporting Information), validating faster ORR kinetics on CNB-ZIL 8 and further suggesting the superior role of interfacial B–N–C species in reducing oxygen. Further insights into the HO_2^- production behavior were given by the corresponding molar selectivity based on RRDE measurements. As can be seen from Figure 4b, the majority of electrons are used along the 2-electron ORR pathway on the CNB-ZIL 8 material, giving a HO_2^- selectivity as high as 85 % with a wide range of potential. In contrast, both CNB-ZIL 9 and 10 catalysts exhibit a much lower peroxide selectivity at any

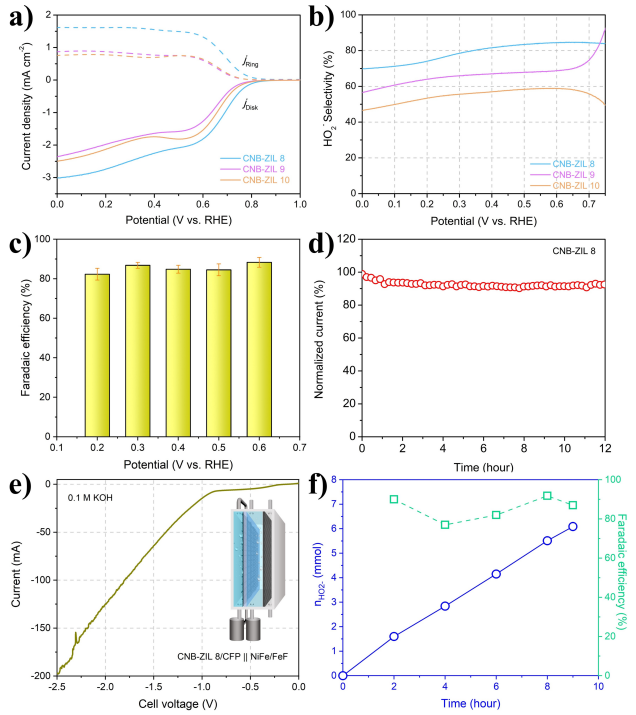

Figure 4. a) RRDE measurements of CNB-ZIL catalysts for ORR in O_2-saturated 0.1 M KOH solution under a rotating rate of 1600 rpm. b) Calculated HO_2^- selectivity on CNB-ZIL samples in O_2-saturated 0.1 M KOH based on the RRDE measurements. c) Faradaic efficiency obtained from chemical titration for the CNB-ZIL 8 in an O_2-saturated 0.1 M KOH electrolyte. d) Long-term electrochemical durability of CNB-ZIL 8 at 0.3 V_{RHE} in O_2-saturated 0.1 M KOH solution. e) Polarization curve of CNB-ZIL 8 loaded CFP electrode in flow cell utilising O_2 at a scan rate of 5 mV s^{-1}. f) The amount of HO_2^- produced (left) and the corresponding faradaic efficiency (right) by CNB-ZIL 8 as a function of electrolysis time under continuous O_2 purging in flow cell.

given potential (Figure 4b), demonstrating the intrinsic active nature of interfacial B–N–C moieties in selectively reducing O_2 to HO_2^-.

To further confirm the important role of highly isolated B–N–C moieties in catalyzing ORR through a $2e^-$ pathway, samples with *h*-BN moiety only (pure boron nitride, BN) and pure nitrogen-doped carbon with a similar N content (NC) were also evaluated. As expected, the NC in the absence of any BNC species exhibits a poor HO_2^- selectivity in O_2-saturated 0.1 M KOH (Figure S9, Supporting Information), where O_2 was mainly reduced along a $4e^-$ pathway ($O_2+2H_2O+4e^-\rightarrow 4OH^-$). Moreover, the selectivity of pure BN catalyst is also much lower than that of CNB-ZIL 8, giving only 72 % and 67 % selectivity to peroxide species at 0.6 V and 0.4 V, respectively, which is similar to that of the control samples with a high *h*-BN content (e.g. CNB-ZIL 9). Thus, comparing the performances of the different catalysts mentioned above, it can be concluded that the high selectivity of CNB-ZIL 8 catalyst toward HO_2^- is mainly attributed to the presence of abundant interfacial B–N–C moieties rather than the *h*-BN species. Notably, previous studies suggest that smaller work function on catalysts could result in lower overpotentials derived from their optimized oxophilicity, thereby a high ORR activity can result.[24,52,53] In this regard, to further rationalize the high $2e^-$ ORR activity on the CNB-ZIL 8, work function (WF) values of CNB-ZIL catalysts were also characterized (Figure S10, Supporting Information). As shown in Figure S10, compared with CNB-ZIL 9 and 10, the CNB-ZIL 8 catalyst exhibits the lowest WF of ≈2.84 eV, indicating a lower energetic barrier to donate electrons from its surface to the dioxygen species (either adsorbed O_2 at the inner Helmholtz plane or $O_2/O_2^{\bullet-}$ redox couple at the outer Helmholtz plane), thereby first facilitating the formation of the OOH species, which is crucial for the subsequent generation of HO_2^-. Moreover, previous theoretical studies demonstrate that the configurations of B heteroatoms have significant impact on the ORR tendency of pyridinic N.[29] Isolated B–N pairs would have a relatively weak adsorption energy towards HO_2^-, which breaks the chain of further reduction of peroxide intermediates within the undesirable $4e^-$ pathway.[29] In contrast, larger *h*-BN domains are not only inactive as ORR catalysts but also electrical insulating which hinders the rapid charge transfer during reaction.[24] Hence, it is the rather homogeneous distribution of abundant interfacial B–N–C moieties in CNB-ZIL 8 that leads to i) a lower WF of catalysts that in turn establishes a lower energy barrier for the reduction of O_2 (as reflected by a slightly lower E_{onset} recorded on CNB-ZIL 8 than that of the reference samples); ii) a high peroxide selectivity that might originate from a weak adsorption of HO_2^- species on those highly isolated B–N–C configurations. This echoes well with the previous observations over ORR process on CNB materials, where paired B–N species are not highly active towards a $4e^-$ pathway but might be responsible for the peroxide generation that has been long ignored.[27,28,31] To exclude the possible role of carbon structural defects in catalyzing ORR, in situ and ex situ Raman measurements were also conducted on CNB-ZIL catalysts (Figure S11, Supporting Information). No obvious structural defects can be identified on CNB-ZIL 8 under any applied ORR potentials, suggesting no interference of carbon defects on the ORR activity.

It is worth noting that the practical bulk electrolysis normally requires powdery catalysts loaded on the hydrophobic carbon fiber supports to enable continuous hydrogen peroxide generation. Therefore, in addition to the RRDE measurements, the HO_2^- performance of CNB-ZIL 8 was further investigated in near-technical bulk electrolysis to evaluate the Faradaic efficiency (FE) and stability of catalyst in H-cell devices with continuous O_2 bubbling. As shown in Figure 4c, the HO_2^- selectivity on the CNB-ZIL 8 catalyst is higher than 80 % within a wide range of potentials from 0.2 V to 0.6 V, echoing with the RRDE results. The slightly higher FE values obtained from H-cell setups compared with the molar selectivity (RRDE measurements) is attributed to the hydrophobic nature of the carbon support, which enables a better wetting with O_2. Further, the ORR current on CNB-ZIL 8 remains almost unchanged within 12-h chronoamperometric test (Figure 4d), indicating a good catalytic durability of the catalyst. Notably, even after a 12-h duration, the FE on CNB-ZIL 8 is still as high as 88 % (Figure S12, Supporting Information), further validating

robustness in terms of catalytic current and selectivity on the CNB-ZIL 8 material. Overall, the above RRDE and H-cell electrolytic tests suggest a high catalytic activity, HO_2^- selectivity, and stability on the CNB-ZIL 8 catalyst, making it an excellent $2e^-$ ORR electrode for practical chemical synthesis.

However, the peroxide generation rate in a static H-cell or RRDE configuration is severely limited by the poor mass transport efficiency (e.g. low O_2 diffusion efficiency and HO_2^- desorption rate), thereby resulting in an unsatisfactory apparent productivity.[54] To this end, the catalytic ORR performance of CNB-ZIL 8 materials toward HO_2^- production was further evaluated in a modified commercial flow-cell reactor (Figure S13, Supporting Information) for continuous bulk electrolysis. During the measurements, the CNB-ZIL 8-loaded carbon fiber electrode and a $Ni_{1-x}Fe_xOH$-loaded iron foam (see details in the Supporting Information) were directly employed as the gas-diffusion cathode and the anode in the flow cell, respectively. As shown in Figure 4e, with an E_{onset} of −0.84 V, the overall cell current increases rapidly along with the increased cell voltage, reaching −200 mA at an uncompensated cell voltage of −2.5 V. This spectacular performance can be ascribed to a several orders of magnitude faster O_2 supply in flow cell than that in conventional H-cell setups. At a cell voltage of −1.4 V, the peroxide species were produced continuously with a generation rate of $\approx 1787\ mmol\, g_{catalyst}^{-1} h^{-1}$ under a j of $\approx 40\ mA\, cm^{-2}$ (Figure S14, Supporting Information). Moreover, a HO_2^- selectivity of above 80 % was maintained without significant drop during the continuous 9-hour electrolysis session (Figure 4f), demonstrating the intrinsically selective nature of CNB-ZIL 8 catalysts that can be even transferred to practical peroxide generation.

Conclusion

In summary, using an IL-assisted doping strategy, turbostratic carbon catalysts with identifiable interfacial boron-nitrogen moieties were fabricated and were applied as efficient $2e^-$ ORR electrocatalysts in alkaline aqueous media. By employing combined X-ray absorption spectroscopy, FTIR and XPS characterizations, we could confirm the presence of abundant, highly dispersed B–N–C configurations in CNB-ZIL 8, while samples obtained from higher pyrolysis temperatures tend to exhibit agglomerated *h*-BN domains, showing distinguishable structure differences that can be correlated to different catalytic behavior. Further conducting electrochemical measurements reveals a positive relationship between the presence of interfacial B–N–C moieties and a high HO_2^- selectivity, giving insights into the origin of peroxide selectivity in boron and nitrogen co-doped carbon catalysts. Benefited from a hierarchical porous feature and well-defined B–N active moieties, the as-prepared CNB-ZIL 8 catalysts can catalyze ORR via a dominant $2e^-$ pathway (up to 85 % selectivity), which was maintained without significant decay for an over 12 h duration. Further employing such catalysts in a flow-cell reactor yields a peroxide generation rate of $1787\ mmol\, g_{catalyst}^{-1} h^{-1}$ at a cell voltage of −1.4 V, demonstrating the practical efficacy of CNB-ZIL 8 in bulk peroxide synthesis. This work also provides insights into the design of B and N co-doped CMs with well-controlled B–N–C configurations, which could be of particular interest for other electrochemical reactions.

Acknowledgements

Z. Tian sincerely acknowledges the financial support provided by the National Natural Science Foundation of China (52003251) and Henan Center for Outstanding Overseas Scientists (GZS2022014). The work was supported by the Australian Renewable Energy Agency (ARENA 2018/RND014), Australian Research Council (ARC) Training Centre for Global Hydrogen Economy (IC200100023), and ARC Research Hub on Integrated Energy Storage Solutions (IH180100020). X. L. acknowledges the UNSW Scientia Scheme for financial support. J. P. also acknowledges the financial support from ARC under the Discovery Early Career Researcher Award DE190100131. Max Planck Society is gratefully acknowledged for the financial and organizational support over many years. Part of this research was undertaken on the SXR beamline at the Australian Synchrotron, ANSTO. Open Access funding enabled and organized by Projekt DEAL.

Conflict of Interest

The authors declare no conflict of interest.

Data Availability Statement

The data that support the findings of this study are available from the corresponding author upon reasonable request.

Keywords: B/N Co-Doping · H_2O_2 Synthesis · Oxygen Reduction Reaction · Turbostratic Carbon

[1] https://www.fortunebusinessinsights.com/hydrogen-peroxide-market-103920, access October 21, 2021.
[2] C. Xia, J. Y. Kim, H. Wang, *Nat. Catal.* **2020**, *3*, 605–607.
[3] C. Xia, Y. Xia, P. Zhu, L. Fan, H. Wang, *Science* **2019**, *366*, 226–231.
[4] Q. Zhang, X. Tan, N. M. Bedford, Z. Han, L. Thomsen, S. Smith, R. Amal, X. Lu, *Nat. Commun.* **2020**, *11*, 4181.
[5] Y. Sun, L. Han, P. Strasser, *Chem. Soc. Rev.* **2020**, *49*, 6605–6631.
[6] S. Yang, A. Verdaguer-Casadevall, L. Arnarson, L. Silvioli, V. Čolić, R. Frydendal, J. Rossmeisl, I. Chorkendorff, I. E. L. Stephens, *ACS Catal.* **2018**, *8*, 4064–4081.
[7] Y. Xia, X. Zhao, C. Xia, Z.-Y. Wu, P. Zhu, J. Y. Kim, X. Bai, G. Gao, Y. Hu, J. Zhong, Y. Liu, H. Wang, *Nat. Commun.* **2021**, *12*, 4225.

[8] N. Wang, S. Ma, P. Zuo, J. Duan, B. Hou, *Adv. Sci.* **2021**, *8*, 2100076.
[9] X. Yang, Y. Zeng, W. Alnoush, Y. Hou, D. Higgins, G. Wu, *Adv. Mater.* **2022**, *34*, 2107954.
[10] M. A. O'Connell, J. R. Lewis, A. J. Wain, *Chem. Commun.* **2015**, 10314–10317.
[11] S. Siahrostami, A. Verdaguer-Casadevall, M. Karamad, D. Deiana, P. Malacrida, B. Wickman, M. Escudero-Escribano, E. A. Paoli, R. Frydendal, T. W. Hansen, I. Chorkendorff, I. E. L. Stephens, J. Rossmeisl, *Nat. Mater.* **2013**, *12*, 1137–1143.
[12] A. Verdaguer-Casadevall, D. Deiana, M. Karamad, S. Siahrostami, P. Malacrida, T. W. Hansen, J. Rossmeisl, I. Chorkendorff, I. E. L. Stephens, *Nano Lett.* **2014**, *14*, 1603–1608.
[13] Y. Bu, Y. Wang, G.-F. Han, Y. Zhao, X. Ge, F. Li, Z. Zhang, Q. Zhong, J.-B. Baek, *Adv. Mater.* **2021**, *33*, 2103266.
[14] Z. Lu, G. Chen, S. Siahrostami, Z. Chen, K. Liu, J. Xie, L. Liao, T. Wu, D. Lin, Y. Liu, T. F. Jaramillo, J. K. Nørskov, Y. Cui, *Nat. Catal.* **2018**, *1*, 156–162.
[15] H. W. Kim, M. B. Ross, N. Kornienko, L. Zhang, J. Guo, P. Yang, B. D. McCloskey, *Nat. Catal.* **2018**, *1*, 282–290.
[16] X. Hu, X. Zeng, Y. Liu, J. Lu, X. Zhang, *Nanoscale* **2020**, *12*, 16008–16027.
[17] T.-P. Fellinger, F. Hasché, P. Strasser, M. Antonietti, *J. Am. Chem. Soc.* **2012**, *134*, 4072–4075.
[18] C. Tang, L. Chen, H. Li, L. Li, Y. Jiao, Y. Zheng, H. Xu, K. Davey, S.-Z. Qiao, *J. Am. Chem. Soc.* **2021**, *143*, 7819–7827.
[19] Y. J. Sa, J. H. Kim, S. H. Joo, *Angew. Chem. Int. Ed.* **2019**, *58*, 1100–1105; *Angew. Chem.* **2019**, *131*, 1112–1117.
[20] K.-H. Wu, D. Wang, X. Lu, X. Zhang, Z. Xie, Y. Liu, B.-J. Su, J.-M. Chen, D.-S. Su, W. Qi, S. Guo, *Chem* **2020**, *6*, 1443–1458.
[21] J. S. Lim, J. H. Kim, J. Woo, D. S. Baek, K. Ihm, T. J. Shin, Y. J. Sa, S. H. Joo, *Chem* **2021**, *7*, 3114–3130.
[22] S. Chen, T. Luo, K. Chen, Y. Lin, J. Fu, K. Liu, C. Cai, Q. Wang, H. Li, X. Li, J. Hu, H. Li, M. Zhu, M. Liu, *Angew. Chem. Int. Ed.* **2021**, *60*, 16607–16614; *Angew. Chem.* **2021**, *133*, 16743–16750.
[23] J. Jin, F. Pan, L. Jiang, X. Fu, A. Liang, Z. Wei, J. Zhang, G. Sun, *ACS Nano* **2014**, *8*, 3313–3321.
[24] J. Wang, J. Hao, D. Liu, S. Qin, D. Portehault, Y. Li, Y. Chen, W. Lei, *ACS Energy Lett.* **2017**, *2*, 306–312.
[25] P. Giusto, H. Arazoe, D. Cruz, P. Lova, T. Heil, T. Aida, M. Antonietti, *J. Am. Chem. Soc.* **2020**, *142*, 20883–20891.
[26] J. Wu, M.-T. F. Rodrigues, R. Vajtai, P. M. Ajayan, *Adv. Mater.* **2016**, *28*, 6239–6246.
[27] S. Wang, E. Iyyamperumal, A. Roy, Y. Xue, D. Yu, L. Dai, *Angew. Chem. Int. Ed.* **2011**, *50*, 11756–11760; *Angew. Chem.* **2011**, *123*, 11960–11964.
[28] S. Wang, L. Zhang, Z. Xia, A. Roy, D. W. Chang, J.-B. Baek, L. Dai, *Angew. Chem. Int. Ed.* **2012**, *51*, 4209–4212; *Angew. Chem.* **2012**, *124*, 4285–4288.
[29] Y. Zheng, Y. Jiao, L. Ge, M. Jaroniec, S. Z. Qiao, *Angew. Chem. Int. Ed.* **2013**, *52*, 3110–3116; *Angew. Chem.* **2013**, *125*, 3192–3198.
[30] M. Fan, Q. Yuan, Y. Zhao, Z. Wang, A. Wang, Y. Liu, K. Sun, J. Wu, L. Wang, J. Jiang, *Adv. Mater.* **2022**, *34*, 2107040.
[31] Y. Zhao, L. Yang, S. Chen, X. Wang, Y. Ma, Q. Wu, Y. Jiang, W. Qian, Z. Hu, *J. Am. Chem. Soc.* **2013**, *135*, 1201–1204.
[32] S. Chen, Z. Chen, S. Siahrostami, D. Higgins, D. Nordlund, D. Sokaras, T. R. Kim, Y. Liu, X. Yan, E. Nilsson, R. Sinclair, J. K. Nørskov, T. F. Jaramillo, Z. Bao, *J. Am. Chem. Soc.* **2018**, *140*, 7851–7859.
[33] Z. Liu, T. B. Marder, *Angew. Chem. Int. Ed.* **2008**, *47*, 242–244; *Angew. Chem.* **2008**, *120*, 248–250.
[34] L. Wang, P. Yu, L. Zhao, C. Tian, D. Zhao, W. Zhou, J. Yin, R. Wang, H. Fu, *Sci. Rep.* **2014**, *4*, 5184.
[35] J. S. Lee, X. Wang, H. Luo, G. A. Baker, S. Dai, *J. Am. Chem. Soc.* **2009**, *131*, 4596–4597.
[36] X. Wang, S. Dai, *Angew. Chem. Int. Ed.* **2010**, *49*, 6664–6668; *Angew. Chem.* **2010**, *122*, 6814–6818.
[37] D. R. MacFarlane, M. Forsyth, P. C. Howlett, M. Kar, S. Passerini, J. M. Pringle, H. Ohno, M. Watanabe, F. Yan, W. Zheng, S. Zhang, J. Zhang, *Nat. Rev. Mater.* **2016**, *1*, 15005.
[38] S. Zhang, K. Dokko, M. Watanabe, *Chem. Mater.* **2014**, *26*, 2915–2926.
[39] X.-H. Li, S. Kurasch, U. Kaiser, M. Antonietti, *Angew. Chem. Int. Ed.* **2012**, *51*, 9689–9692; *Angew. Chem.* **2012**, *124*, 9827–9830.
[40] S. Tröger-Müller, M. Antonietti, C. Liedel, *Phys. Chem. Chem. Phys.* **2018**, *20*, 11437–11443.
[41] S. Zhang, K. Dokko, M. Watanabe, *Mater. Horiz.* **2015**, *2*, 168–197.
[42] J. Park, Y. Nabae, T. Hayakawa, M.-a. Kakimoto, *ACS Catal.* **2014**, *4*, 3749–3754.
[43] C. N. R. Rao, K. Pramoda, *Bull. Chem. Soc. Jpn.* **2019**, *92*, 441–468.
[44] D. Zhao, Y. Wang, C.-L. Dong, Y.-C. Huang, J. Chen, F. Xue, S. Shen, L. Guo, *Nat. Energy* **2021**, *6*, 388–397.
[45] S. M. Kim, A. Hsu, P. T. Araujo, Y.-H. Lee, T. Palacios, M. Dresselhaus, J.-C. Idrobo, K. K. Kim, J. Kong, *Nano Lett.* **2013**, *13*, 933–941.
[46] Y. Gong, H. Fei, X. Zou, W. Zhou, S. Yang, G. Ye, Z. Liu, Z. Peng, J. Lou, R. Vajtai, B. I. Yakobson, J. M. Tour, P. M. Ajayan, *Chem. Mater.* **2015**, *27*, 1181–1186.
[47] L. Ci, L. Song, C. Jin, D. Jariwala, D. Wu, Y. Li, A. Srivastava, Z. F. Wang, K. Storr, L. Balicas, F. Liu, P. M. Ajayan, *Nat. Mater.* **2010**, *9*, 430–435.
[48] A. A. Makarova, L. Fernandez, D. Y. Usachov, A. Fedorov, K. A. Bokai, D. A. Smirnov, C. Laubschat, D. V. Vyalikh, F. Schiller, J. E. Ortega, *J. Phys. Chem. C* **2019**, *123*, 593–602.
[49] D. Li, G. M. Bancroft, M. E. Fleet, *J. Electron Spectrosc. Relat. Phenom.* **1996**, *79*, 71–73.
[50] R. Peter, A. Bozanic, M. Petravic, Y. Chen, L. J. Fan, Y. W. Yang, *J. Appl. Phys.* **2009**, *106*, 083523.
[51] X. Li, W. Hua, B.-Y. Wang, W.-F. Pong, P.-A. Glans, J. Guo, Y. Luo, *Appl. Phys. Lett.* **2016**, *109*, 081601.
[52] M. Sharma, J.-H. Jang, D. Y. Shin, J. A. Kwon, D.-H. Lim, D. Choi, H. Sung, J. Jang, S.-Y. Lee, K. Y. Lee, H.-Y. Park, N. Jung, S. J. Yoo, *Energy Environ. Sci.* **2019**, *12*, 2200–2211.
[53] L. Yang, J. Shui, L. Du, Y. Shao, J. Liu, L. Dai, Z. Hu, *Adv. Mater.* **2019**, *31*, 1804799.
[54] E. Jung, H. Shin, W. Hooch Antink, Y.-E. Sung, T. Hyeon, *ACS Energy Lett.* **2020**, *5*, 1881–1892.

Manuscript received: May 11, 2022
Accepted manuscript online: July 27, 2022
Version of record online: August 8, 2022